



Continuous synthesis of nickel nanopowders: Characterization, process optimization, and catalytic properties



Mattia Alberto Lucchini^{a,b}, Andrea Testino^{b,*}, Christian Ludwig^{b,d}, Anastasios Kambolis^b, Mario El-Kazzi^b, Antonio Cervellino^c, Paola Riani^a, Fabio Canepa^a

^a Department of Chemistry and Industrial Chemistry, University of Genoa, Via Dodecaneso 31, 16142 Genoa, Italy

^b Paul Scherrer Institut (PSI), ENE-LBK, 5232 Villigen PSI, Switzerland

^c Swiss Light Source, Paul Scherrer Institut, 5232 Villigen PSI, Switzerland

^d École Polytechnique Fédérale de Lausanne (EPFL), ENAC-IIE, 1015 Lausanne, Switzerland

ARTICLE INFO

Article history:

Received 18 January 2014

Received in revised form 20 March 2014

Accepted 22 March 2014

Available online 30 March 2014

Keywords:

Nickel nanoparticles

Continuous synthesis

CO methanation

Segmented Flow Tubular Reactor

ABSTRACT

The preparation of nanoparticles with tailored properties and in quantities in the order of 10–100 g prepared with laboratory-scale equipment is a target of great interest. In this study, Ni nanoparticles with different sizes, surface morphologies, magnetic, and catalytic properties were obtained from NiCl_2 , N_2H_4 , NaOH, and ethylene glycol as solvent by tuning the synthesis parameters. Preliminary syntheses were done in batch reactors and then the continuous synthesis carried out in the Segmented Flow Tubular Reactor (SFTR). For the first time a SFTR system was applied to a non-aqueous system. By combining SEM, HRTEM, XRD, TGA, XPS, FTIR, specific surface area, SQUID, and catalytic tests, the complete structural, morphological, and functional characterization of the produced nanoparticles were performed. The continuous production of 2.1 g h^{-1} of Ni nanoparticles was carried out up to 6 h without product properties deterioration. The results allow estimating a production $>300 \text{ g d}^{-1}$ in an *ad-hoc* low-cost single-tube SFTR system. Catalytic tests of CO methanation showed good activity at 769 K with stable methane yield of 83%. The results presented in this study demonstrate that reliable and reproducible synthesis of relatively high amounts of metal nanoparticles with lab-scale equipment can be achieved. This approach opens new opportunities for reliable and controlled preparation of advanced materials in quantities suitable for a full functional characterization.

© 2014 Elsevier B.V. All rights reserved.

1. Introduction

Metal nanoparticles (NPs) have attracted much interest in the last years due to their unique properties and applications in several areas such as microelectronics, catalysis, and biomedicine [1,2]. Specifically, magnetic nanoparticles have potential applications as ferrofluids [3], magnetic retrievable catalysts [4–6] and photocatalysts [7], magnetic carriers for drug targeting [8,9] and hyperthermia [10].

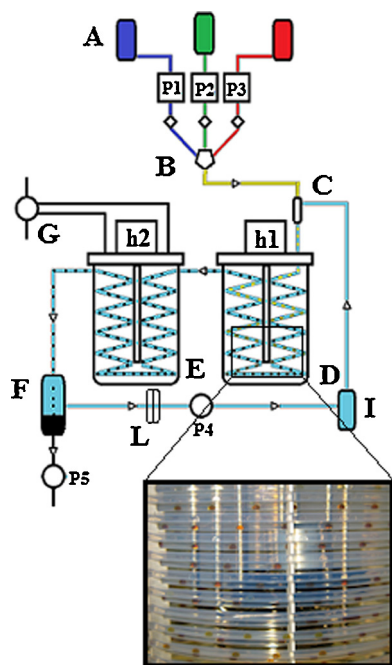
Pure and supported Ni NPs have promising catalytic properties. Double bond hydrogenation, carbon dioxide hydration, CO methanation [11,12], and ethanol steam reforming reactions were reported [13–17]. Moreover, the interest in massive production of fine nickel powders as substitute for noble metals in

microelectronics, such as in the base-metal-electrode multi-layer ceramic capacitors (BME-MLCCs), is rapidly growing. In these miniaturized devices, since materials prepared by top-down techniques are approaching the technical limitations, bottom-up methods are more and more attractive [18,19].

Most physical and chemical properties of nanoparticles strongly depend on their size and shape. Several synthesis methods were developed to obtain Ni NPs with well-defined dimension, narrow size distribution, and limited particle aggregation. Solvothermal reduction [20], thermal decomposition [21,22], microwave assisted reduction [23,24], laser ablation [25], irradiation [26], aqueous [27–29] and polyol synthesis routes [30–32] are some of the possible methods.

Although the aforementioned methods allow obtaining satisfying products, the reported productions are often limited to few milligrams and are carried out in lab-scale batch reactors. Laboratory prepared powders are often very difficult to scale-up maintaining the product quality. Thus, the reproducible synthesis

* Corresponding author. Tel.: +41 (0) 56 310 5449; fax: +41 (0) 56 310 2199.
E-mail address: andrea.testino@psi.ch (A. Testino).



Scheme 1. Sketch of the SFTR reactor. A: pumping system composed by three HPLC pumps (P1, P2, P3) pulsation dumpers and back pressure valves; B: mixer; C: segmenter; D: thermostatic bath equipped with heating head (H1) and mechanical stirrer; E: cooling bath equipped with heating head (H2) and mechanical stirrer and connected to the chiller (G); F: decanter connected to the pump P5; I: reservoir; L: filter; P4: circulating pump.

of nanopowders with desired shape, particle size distributions, stoichiometry, crystalline phase, and in a considerable amount is still a major concern.

In general, chemical solution methods have shown the capability to control composition, size and shape, and are suitable for up-scaling. Among the solution methods, the reduction of inorganic Ni^{2+} salts by hydrazine, with NaOH as promoting agent, in absence of polymeric additives, and using ethylene glycol (EG) as solvent, is a convenient method for Ni NPs preparation. Moreover, according to this method (i) pure Ni is directly produced; (ii) the product has high surface area due to the small primary particle size and particle surface roughness; (iii) the particles surface is not polymer-coated and suitable for catalytic processes without additional thermal treatments; (iv) it does not require expensive chemicals; (v) it is scalable; (vi) has no byproducts difficult to remove or hazardous; (vii) it is rather fast; (viii) it is possible to use high metal salts concentration; (ix) to a certain extent size and morphological control is achievable [33–35]. Only few papers report on continuous methods [36] or larger quantities but in batch reactors [37].

Over recent years a new type of tubular plug flow reactor – the Segmented Flow Tubular Reactor (SFTR) – has been conceived and used in powder synthesis [38]. This type of reactor has shown excellent performances, versatility and robustness through the preparation of different products: CaCO_3 [39], BaTiO_3 [40], copper oxalate, calcium and nickel-manganese oxalates [41,42] with a high powder quality (chemical and phase composition, narrow particle size distribution, and controlled shape) and reproducibility [43]. The SFTR was developed to overcome the classical problems of up-scaling powder production from batch processes, which are mainly linked with mixing, homogeneity, and heat transfer. A schematic view of the SFTR is given in Scheme 1. The SFTR is composed of three distinct parts: (i) a micromixer which ensures that the reactants are efficiently mixed, (ii) a segmenter, and (iii)

a tubular reactor, placed in a thermostatic bath. Small suspension volumes (about 0.2 cm^3) are thus created, producing microdroplets or microreactors in an immiscible fluid, where the reaction – in this case Ni^{2+} reduction and Ni precipitation – takes place. These small volumes ensure a high homogeneity inside each droplet, all circulating through the tube with an identical history (e.g., residence time and heat exchange). The reaction or the precipitation occurs in the mixing chamber and/or is induced by the rapid temperature change when the microreactors are heated in the thermostatic bath. According to fluid dynamic modeling, the temperature of the droplets reaches 95% and 99% of the bath temperature within 6 and 10 s, respectively [44]. Fouling on the inner tubular reactor wall is avoided due to the immiscible fluid by forming a thin film on the tube surface [45] and thus allowing long continuous process times ($>12 \text{ h}$). The residence time is determined by the pump flow rates and the tube length and adjusted according to the specific reaction kinetics. This is a steady-state process in which each step, mixing and reaction, is well separated, leading to a better control and reproducibility. If needed, after the tubular reactor, in the process line, a heat-exchanger can be placed to cool down the reacting mixture and quench the reaction. Finally, a separation unit or decanter allows the separation of the product by the immiscible fluid; the product – particle in suspension – is collected, while the immiscible fluid is recycled in the process for environmental and cost concerns. To increase productivity for commercial application, the SFTR can be “scaled-out” by multiplying the number of tubes running in parallel instead of scaling-up by increasing their size. The production of calcium carbonate with a scaling-out factor of 5000 with no change in product quality and the robustness of the process in the production of high quality ultrafine barium titanate powders were already demonstrated [46].

This work reports the continuous synthesis of Ni NPs in the SFTR reactor. For the first time, a polyol synthesis was studied and successfully carried out in the SFTR reactor, extending the portfolio of possible applications towards non-aqueous systems and up to the EG boiling temperature. Systematic investigation of the synthesis parameters for Ni NPs preparation such as precursor concentration, temperature, reaction time, for both small batch and continuous SFTR processes are presented. Selected batch samples and the most relevant SFTR products were morphologically, spectroscopically and magnetically characterized. Moreover, thermal and catalytic properties of selected pure Ni samples are presented. With a single tube SFTR reactor, the continuous production of Ni NPs up to 2.1 g h^{-1} has been achieved with constant product properties over the time frame tested (6 h), proving the potential of the SFTR not only at laboratory scale.

2. Experimental

2.1. Materials

Nickel chloride hexahydrate ($\text{NiCl}_2 \cdot 6\text{H}_2\text{O}$, $>98\%$), hydrazine monohydrate ($\text{N}_2\text{H}_4 \cdot \text{H}_2\text{O}$, 65%, reagent grade 98%), sodium hydroxide (NaOH, $>98\%$), ethylene glycol (EG, puriss. p.a. $>99.5\%$), *n*-dodecane ($n\text{-C}_{12}$, reagent grade, $>99\%$), and Ni nanopowders – named A01 in the following text – as benchmark (Ni, #577995, declared particle size $<100 \text{ nm}$, $>99\%$) were obtained from Sigma–Aldrich and used as received without further purification. Ethanol and acetone used for powder washing purpose were reagent grade and obtained from VWR. $\gamma\text{-Al}_2\text{O}_3$ (Sasol Puralox) was used to dilute Ni particles for catalytic tests.

Few tests were carried out with polymeric additives: Na-polyacrylate (Na-PA, Sigma–Aldrich, AMW = 8k) and polyvinylpyrrolidone (PVP, Sigma–Aldrich, AMW = 40k).

2.2. Batch synthesis

NaOH was dissolved in EG at 333 K and cooled to RT. $\text{NiCl}_2 \cdot 6\text{H}_2\text{O}$ was dissolved in EG in a three-neck flask. Then, pure $\text{N}_2\text{H}_4 \cdot \text{H}_2\text{O}$ was added to the flask; one minute later, the NaOH solution was added as well. The precursor mixture was prepared at room temperature and was kept under vigorous mechanical stirring. At this stage the precursor mixture was light blue and turbid due to the formation of $\text{Ni-N}_2\text{H}_4$ complex [36,47,48]. The three-neck flask was dipped in a preheated oil bath at the reaction temperature and kept stirred for the entire reaction time. The precursor mixture turns black after a few minutes. The product was washed three times with ethanol and once with acetone. Ni powders were magnetically retrieved from the solution and sonicated (Sonics – VIBRA CELL, VCX130, 130 W 20 kHz, 50% power, 1.5 min) between each washing step. Finally, the powders were dried in air at RT and stored in closed vials.

In this paper, samples named as *Bn* concern particles prepared in batch reactor. The synthesis parameters investigated for batch syntheses were: reactants concentration (C_{Ni} , $C_{\text{N}_2\text{H}_4}$, and C_{NaOH}), overall volume (V_T), and reaction time (t_R). Unless otherwise specified, the reaction temperature (T_R) was kept at 393 K. Table S1 (Supporting Information) summarizes a selection of the experimental conditions tested.

2.3. Continuous synthesis in the Segmented Flow Tubular Reactor (SFTR)

Scheme 1 shows the SFTR used for the Ni NPs production. The system is composed of three HPLC pumps, each equipped with a pulsation damper and a back pressure valves. In the frame of this experimental work, the pressure was kept at about 30 MPa. Pump 1 (P1) was used to deliver the Ni^{2+} precursor solution in EG; pump 2 (P2) was used for a solution of NaOH and N_2H_4 in EG; pump 3 (P3) was for pure EG. The accuracy of the pumps flow rate was gravimetrically controlled. The three solutions were mixed in a cross-mixer at RT. The precursor mixture was fed to a segmenter, where the EG-based mixture was divided into droplets separated by a flow of an immiscible fluid ($n\text{-C}_{12}$) provided by a gear pump (P4). The segmented fluid was pumped in a Teflon tube (4 mm i.d.). The tube was kept in a silicon oil thermostatic bath at the reaction temperature (T_R). In a second thermostatic bath, the segmented fluid was quenched at $T = 278$ K. After cooling, the EG-based suspension was separated from the $n\text{-C}_{12}$ in a decanter; $n\text{-C}_{12}$ was filtered and recirculated, while the EG-based suspension, which contains the product, was continuously withdrawn by a peristaltic pump (P5). The overall systems worked with only one level control – applied at the decanter – which adjusts the flow rate of P5.

Aging time, (t_A), i.e. the time in which the segmented fluid was kept at T_R , was tuned by pumps flow rate (P1–P4) ($t_A = V_R/F_{P1 \dots P4}$, where V_R is the tubular reactor volume kept at T_R and $F_{P1 \dots P4}$ is the overall flow rate of P1–P4). The products were washed and stored as described for batch samples.

In this paper, samples named as *Sn* concern particles prepared in SFTR reactor. The synthesis parameters investigated for SFTR syntheses were: reactants concentration (C_{Ni} , $C_{\text{N}_2\text{H}_4}$, and C_{NaOH}), T_R , and t_A . Table S2 (Supporting Information) summarizes a selection of the experimental conditions tested.

2.4. Catalyst preparation

A mixture of dried Ni NPs and $\gamma\text{-Al}_2\text{O}_3$ (40:60 by weight) were placed in a glass vial with 15 ml of *i*-propanol and sonicated (Sonics – VIBRA CELL, VCX130, 130 W 20 kHz, 100% power, 1.5 min). After sedimentation, the solvent was removed and the powder dried at RT.

2.5. Powders characterization

For screening purpose, X-ray powder diffraction (XRD) patterns were collected with a Bruker D8 Advance diffractometer (Cu $K\alpha$ radiation) in the range $15\text{--}90^\circ 2\theta$ ($\Delta 2\theta = 0.019^\circ$), while cell parameters and crystallite size were calculated from high resolution X-ray powder diffraction patterns collected using 25 keV synchrotron radiation at the MS-X04SA beamline (SLS-PSI) [49], using 0.3 mm capillary. Cell parameters (a , reported in Table 1) were calculated by Rietveld refinement using GSAS [50] and ICSD [51] database. Crystallite size (d_{XRD}) and microstrain broadening (S_s) were estimated from the refinement using the profile function #4 [52] as well as from the broadening of the first six peaks by means of the Scherrer equation (after correction for instrumental broadening)

$$d_{\text{XRD}} = \frac{K\lambda}{\beta \cos \theta} \quad (1)$$

where K is a dimensionless shape factor (a value of 0.89 was used), λ is the X-ray wavelength, and β and θ are the full width at half maximum (FWHM) and the angle at the maximum intensity of the considered diffraction peak, respectively.

Transmission electron microscopy (TEM) study of the material was performed on a JEOL 2010 with an acceleration voltage of 200 keV, equipped with a LaB_6 filament, an Oxford Instrument energy dispersive X-ray spectrometer (EDS), using INCA software and a CCD camera (Orius from GATAN). A single tilt holder was used. The powders were suspended in *i*-propanol, and a 5 μl drop of this suspension was deposited on a holey carbon film supported on 3 mm copper grid for TEM investigation.

Field Emission Scanning Electron Microscopy (FE-SEM) observations were performed using a Zeiss SUPRA 40 VP instrument, equipped with an energy dispersive X-ray spectrometer (EDX-OXFORD “INCA Energie 450 \times 3”) for microanalysis. The secondary particle size distributions were obtained from SEM images counting at least 200 particles. From the distribution, the average secondary particle size (d_{SEM}) and the coefficient of variance ($\text{CV} = \text{SD}/d_{\text{SEM}}$) were calculated.

Specific surface area (BET method [53], A_{BET}) and pore size distribution (BJH method, desorptions branch [54]) were determined by nitrogen physisorption using a Micromeritics Tristar II 3020 working at 77 K, after evacuation of the sample at 383 K for 72 h.

The BET equivalent diameter (d_{BET}) was obtained using the relation:

$$d_{\text{BET}} = \frac{6}{\rho_{\text{XRD}} A_{\text{BET}}} \quad (2)$$

where ρ_{XRD} is the density measured from lattice parameters and 6 is the geometrical factor for spherical or cubic particles.

Magnetic measurements were carried out in a DC-superconducting quantum interference device (SQUID) magnetometer (MPMS magnetic properties measurement system, Quantum Design). The room temperature magnetic hysteresis cycle was measured with a magnetic field ($\mu_0 H$) in the range -5 to $+5$ T. The thermal dependence of the magnetization ($H = 100$ Oe, $T = 5\text{--}300$ K range) was obtained with the zero field cooling-field cooling (ZFC-FC) procedure. In case of superparamagnetic samples, the magnetization curve was fitted following the Langevin theory:

$$\begin{cases} M(H) = \int_a^b M_s L(r) f(r) dr \\ L(r) = \coth\left(\frac{\mu(r)H}{k_B T}\right) - \frac{k_B T}{\mu(r)H} \end{cases} \quad (3)$$

where, M_s is the saturation magnetization, r is the particle radius, $\mu(r)$ is the particle magnetic moment, k_B is the Boltzmann constant, H is the magnetic field, T is the absolute temperature, and a and b

Table 1

Summary of analytical results (XRD, SEM, and SSA) *a*: lattice parameter; ρ_{XRD} : XRD density; d_{XRD} : crystallite size calculated with GSAS; d_{SEM} : average secondary particle size from SEM images; CV%: coefficient of variation; A_{BET} : specific surface area, BET model; d_{BET} : particle size calculated from A_{BET} ; morphol: qualitative particle morphology.

Sample #	<i>a</i> (Å)	ρ_{XRD} (g cm ⁻³)	d_{XRD} (nm)	d_{SEM} (SD) (nm)	CV%	A_{BET} (m ² g ⁻¹)	d_{BET} (nm)	Morph	$d_{\text{BET}}/d_{\text{XRD}}$	$d_{\text{SEM}}/d_{\text{BET}}$
S02	3.5301	8.863	10.90	60 (8)	13.3	51.7	13.09	Spiky	1.20	4.58
S18	3.5316	8.854	6.89	191 (28)	14.2	5.7	117.6	Raspberry	17.08	1.85
S21	3.5315	8.852	6.85	167 (16)	11.5	9.9	68.47	Raspberry	9.99	2.41
S22	3.5302	8.862	12.63	178 (36)	20.3	27.4	24.74	Spiky	1.96	7.19
S23	3.5301	8.863	11.91	183 (21)	12.7	30.6	22.15	Spiky	1.86	8.26
S26	3.5301	8.864	6.89	163 (22)	12.2	7	96.23	Raspberry	13.97	1.92
B04	3.5302	8.862	19.79	150 (15)	10.1	<i>n.d.</i>	<i>n.d.</i>	Spiky	<i>n.d.</i>	<i>n.d.</i>

are the integral limits (0.01 and 25 nm, respectively). $f(r)$ is the log normal distribution of radii, typical for most nanoparticles, given by Eq. (4):

$$f(r) = \frac{1}{r \cdot \sigma \cdot \sqrt{2\pi}} \cdot \exp \left[-\frac{(\ln r/r_m)^2}{2 \cdot \sigma^2} \right] \quad (4)$$

where r_m is the mean radius and σ is the distribution width.

FTIR measurements were performed using a Bruker Hyperion 3000 microscope coupled to a Bruker Vertex70v Interferometer. Solid samples were deposited on a single ZnSe optical window and measured in transmission mode with 15x Schwarzschild objectives. Liquid samples (e.g. EG as reference measurements) were pressed between two ZnSe optical windows and measured as a thin film in transmission mode with 15x Schwarzschild objectives. The blades of the confocal apertures of the microscope were set at $46 \times 50 \mu\text{m}^2$ for solid samples and at $110 \times 100 \mu\text{m}^2$ for liquid samples. The interferometer was operated in the Mid Infrared region using a Ge Multiplayer beamsplitter supported on KBr. Mirrors were scanned at 40 kHz up to a resolution of 4 cm^{-1} . 500 forward-backward double sided interferograms were collected for background and sample over the range $400\text{--}8000 \text{ cm}^{-1}$, phase corrected with the Mertz method and apodized with a Blackman–Harris 3-Term function and a zero-filling factor of 2.

XPS (X-Ray Photoelectron Spectroscopy) measurements were performed using a VG ESCALAB 220iXL spectrometer (Thermo Fisher Scientific) using a focused Al K α mono-source (spot size: $500 \mu\text{m}$, power: 150 W) and a magnetic lens system. The spectra were recorded in constant analyzer energy mode at pass energy of 50 eV for survey spectra and 30 eV for higher resolution acquisition of core levels. The XPS system was calibrated using the Ag 3d_{5/2}, the Cu 2p_{3/2} and the Au 4f_{7/2} peaks after Ar ion sputtering of the samples surface. The FWHM of the Ag 3d_{5/2} peak is 0.62 eV and 0.76 eV at pass energy of 20 eV and 30 eV, respectively. The data was evaluated using the Advantage software (v. 4.43, Thermo Fisher Scientific). Background subtraction has been performed according to Shirley [55].

Catalytic performance (CO methanation) of the prepared mixture materials was evaluated in a fixed bed reactor (internal diameter 6 mm) operating at atmospheric pressure. For the tests, 250 mg of the catalyst mixture was placed between quartz wool in a quartz tube. The catalyst was pre-treated at 523 K (heating rate 20 K min^{-1}) in 5% H₂ in N₂ in order to completely reduce the Ni NPs surface. The calculated GHSV was $60,000 \text{ ml g}_{\text{Ni}}^{-1} \text{ s}^{-1}$. Then, a mixture of 25% H₂ and 5% CO in N₂ was fed to the reactor (100 ml min^{-1}). The activity of the catalysts was recorded from 523 K to the nominal maximum temperature (593, 623, 723, and 773 K, holding time 15 min) and cooled down to 523 K. This cycle was also repeated for a second time. Feed and reaction products were analyzed using a Thermo Scientific Antaris IGS FTIR spectrometer.

Thermogravimetric analysis (TGA) was carried out with a Mettler Toledo TGA/SDTA 851e in the temperature range 298–773 K (heating rate 5 K min^{-1}). About 20 mg of Ni powders were firstly oxidized

to NiO under Ar/O₂ (20% O₂, 15 ml min^{-1}) atmosphere heating up to 773 K and then cooled down to RT. The flowing gas was then switched to Ar/H₂ (5% H₂, 10 ml min^{-1}) and the sample heated up to 773 K in order to reduce the sample to Ni. The oxidation–reduction cycles were repeated up to four times.

3. Results and discussion

Synthesis conditions, a summary of relevant characteristics, and few notes on particles shape, surface morphology, and observations during the syntheses of selected samples, 13 for batch (B series) and 26 for SFTR (S series) products, are reported in Tables S1 and S2 (Supporting Information).

The explorative tests carried out in batch were used to define the most relevant parameters – and their value ranges – for the continuous synthesis. The target of the continuous production was the preparation of single phase, size and morphology controlled Ni NPs in the scale size of 3 g h^{-1} . Thus, experiments were driven towards rather high precursor concentration, short reaction time, and single phase product. In the SFTR reactor the synthesis conditions may be achieved by tuning the flow rate of pumps P1 and P2 to the target N₂H₄/Ni ratio, of P3 to the target C_{Ni}, and of P4 to the target t_A . T_R is independently set by the thermostatic bath (Scheme 1). Most of the experiments were carried out using the same Ni²⁺ and N₂H₄ mother solutions to avoid batch-to-batch variability and a fast switch among synthesis conditions by setting new flow rates values for P1, P2, P3, and P4. In some cases, for instance for low C_{Ni} in combination with long t_A values, more diluted precursor solutions were prepared.

In the Sections 3.1 and 3.2 the qualitative description of the major results for batch and SFTR prepared samples, respectively, are discussed. A further selection of seven samples, among the B and S series and the sample A01 were morphologically, spectroscopically, and magnetically characterized and discussed in detail in the Section 3.3. Thermal analysis and catalytic tests are reported as well.

3.1. Preliminary batch syntheses: study of qualitative trends

As shown in Table S1 (Supporting Information), at $T_R = 393 \text{ K}$ the reaction is complete for $C_{\text{Ni}} \geq 1 \times 10^{-3} \text{ M}$, while at $T_R = 333 \text{ K}$ the reaction is still incomplete for $C_{\text{Ni}} = 2.5 \times 10^{-3} \text{ M}$ (B09), even for very long t_R ($t_R = 360 \text{ min}$). At $T_R = 393 \text{ K}$ and $C_{\text{Ni}} < 1 \times 10^{-3} \text{ M}$ (B08, no precipitation; B10 few intersecting spheres) the system is poorly reproducible and the reaction volume (i.e., the mixing condition and heterogeneous nucleation on reactor wall) may play a relevant role as well. For instance sample B10 (Fig. S1a, Supporting Information), was difficult to reproduce in size and morphology, XRD-pure Ni phase was not always obtained, and dark deposits on the flask wall was not systematically detected. At $T_R = 393 \text{ K}$ and $1 \times 10^{-3} \text{ M} \leq C_{\text{Ni}} \leq 5 \times 10^{-3} \text{ M}$ the product consists of long wires of several μm length and about 130 nm width (e.g. B01 and B02, Fig. S1b–c, Supporting Information). In this concentration range, the particle surface morphology changed too: at lower concentrations

the particle surface is smooth, while it is rougher for higher concentrations.

Qualitatively, at $T_R = 393$ K and $C_{Ni} = 5 \times 10^{-2}$ M (e.g., B04, B06, B07, B11 (i–iii)) the products show large variance: for instance B11 and B04 were prepared with minor differences (such as V_T) but particle size are not consistent. Among this series, it is difficult to find a rational, demonstrating that batch reactor syntheses are very sensitive to minor parameters. As discussed later (Section 3.2), the reaction temperature has relevant and complex effect on particle size. In the experimental batch conditions, the reaction starts during heating: heating rate depends on overall volume, flask size, mixing condition, evolved gaseous species, and so on. This could be the reason of the initial experimental reproducibility difficulties.

Nevertheless, at $T_R = 393$ K a systematic trend on particle morphology against C_{Ni} may be lined out: the morphology changes from smooth intersecting spheres (B10: $C_{Ni} = 5 \times 10^{-4}$ M, Fig. S1a, Supporting Information), to long wires (B02: $C_{Ni} = 1 \times 10^{-3}$ M, Fig. S1c, Supporting Information), to spherical well-defined particles (B04: $C_{Ni} = 5 \times 10^{-2}$ M, Section 3.3.1, Fig. 2h).

Two syntheses (B03 and B05) were carried out in the presence of Na-PA and PVP, respectively. When Na-PA was used, the reaction did not occur, in agreement with the results of Chou and Huang [27]. PVP was tested as stabilizing agent but no relevant effects were detected on secondary particle size or suspension stability, in contradiction with previously reported results [56].

As a result of this experimental screening C_{Ni} , T_R , t_A , and N_2H_4/Ni were considered as key synthesis parameters and the condition to obtain reproducible results were identified. Sample B04 was characterized in more details and discussed in Section 3.3. This sample was prepared according to the same conditions reported by Eluri and Paul [36] and selected because it may be prepared in a reproducible way.

3.2. Continuous synthesis

In agreement with the batch experiments, for $C_{Ni} \leq 2.5 \times 10^{-2}$ M, Ni^{2+} reduction did not occur (or occurred only partially) even for $T_R = 368$ K (Table S2, Supporting information, S10, S05, S06). Moreover, the reaction did not occur at $T_R \leq 313$ K even for long t_A and high C_{Ni} (sample S14: $t_A = 11.9$ min, $C_{Ni} = 5 \times 10^{-2}$ M). At $T_R \geq 343$ K, a rather high N_2H_4/Ni ratio was required ($N_2H_4/Ni = 20$), otherwise the reaction was not complete for $t_R \leq 4$ min (S12: $N_2H_4/Ni = 10$ and S13: $N_2H_4/Ni = 5$).

For $C_{Ni} = 5 \times 10^{-2}$ M and $T_R = 323$ K the reaction was incomplete and secondary phases were detected by XRD (sample S15: $t_A = 11.8$ min, $C_{Ni} = 5 \times 10^{-2}$ M) while for $T_R \geq 333$ K single phase Ni was obtained (S16: $t_A = 11.8$ min, $C_{Ni} = 5 \times 10^{-2}$ M).

In case of incomplete reaction, secondary phases in the XRD were detectable, in agreement with finding of Park et al. [57]. For single phase Ni as product, the reaction yield was always >95% (gravimetrically measured). It can be concluded that the condition required to achieve full reduction are $T_R \geq 333$ K, $C_{Ni} \geq 0.05$ M, $t_A \geq 5$ min, and $N_2H_4/Ni \geq 3$, in general agreement with the batch experiments.

For $T_R = 343$ K and $N_2H_4/Ni = 20$, the product consists of spherical particles with a rough spiky surface and a decreasing dimension as C_{Ni} increases, from 139 nm to 59 nm for C_{Ni} from 5.5×10^{-3} M to 5×10^{-2} M (Fig. 1a, S01, S02, S03, S04, S09). In the same concentration range but for higher temperature ($T_R = 368$ K), the opposite trend is revealed: d_{SEM} increases from 85 nm to 183 nm (Fig. 1b, S07, S08, S11, S22, S23). Finally, plotting size against T_R (S01, S02, S03, S17, S22, S23, Fig. S2, Supporting Information) at constant N_2H_4/Ni and C_{Ni} (20 and 5×10^{-2} M, respectively), a non-trivial behavior could be found: for $T_R = 343$ K the product consists of spherical spiky particles with d_{SEM} of 59 nm, at $T_R = 368$ K, d_{SEM} is about 180 nm, and

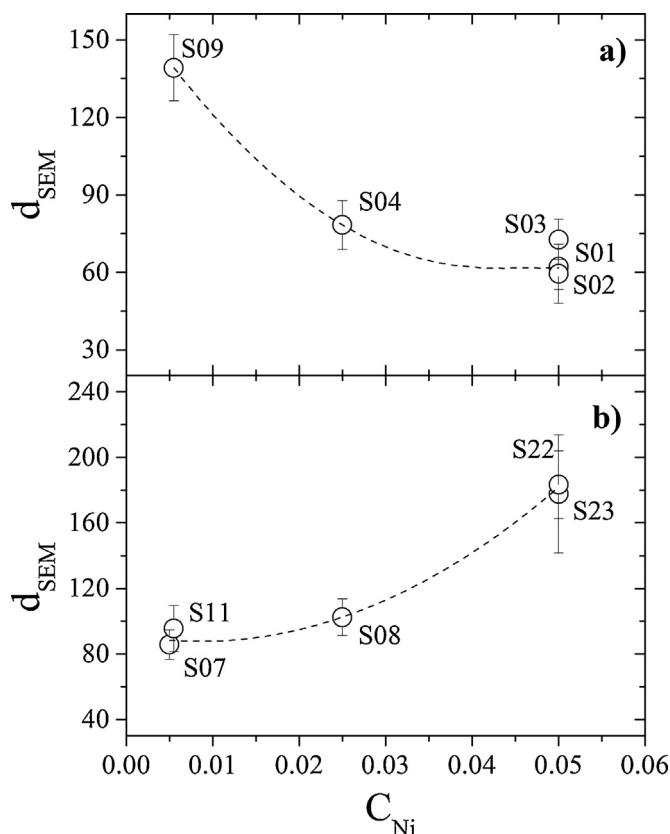
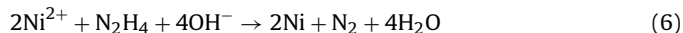


Fig. 1. Average particle size obtained by SEM images (d_{SEM}) against C_{Ni} for molar ratio $N_2H_4/Ni = 20$ and (a) $T_R = 343$ K and (b) $T_R = 368$ K. The bars represent the interval 2sd. The dotted lines serve as eye guide only.

a further temperature increase – up to 403 K – has no influence on particle size.

Intuitively, with an increase of temperature and reactants concentration (C_{Ni} and N_2H_4), a higher driving force for the reduction and smaller particles should be obtained. The behavior shown in Fig. 1 (and Fig. S2, Supporting Information), might be a consequence of the competitive N_2H_4 thermal decomposition reaction (promoted by a metal catalyst, Eq. (5)) with the Ni^{2+} reduction (Eq. (6)) [57].



Experimentally, relevant gas evolution in the SFTR was observed for $T_R > 343$ K. After the decanter, the gases were piped under the fume hood; qualitatively, the evolved gases had a clear basic reaction in agreement with the Eq. (5). At $T_R < 343$ K the thermal decomposition was relatively slower compared to the Ni^{2+} reduction and a higher fraction of N_2H_4 was available, promoting the precipitation of smaller particles. At $T_R \geq 368$ K reactions of Eq. (5) became more important, a lower amount of N_2H_4 was available for the reduction, and the obtained particles were relatively larger. It is worth noting that the particle formation path is not known and the described hypothesis should be supported by a detailed kinetic study on the crystallization mechanism. In analogy to other magnetic systems – and supported by the fact that the particles clearly show a complex sub-structure (Section 3.3.1) – a non-classical crystallization path might be plausible [58]. Moreover, the precipitation kinetics, and as a consequence the secondary particle size obtained, might be influenced by the intermediate solid phases $Ni-N_2H_4-H_2O-Cl^-$ [57]. The study of the precipitation mechanism was not in

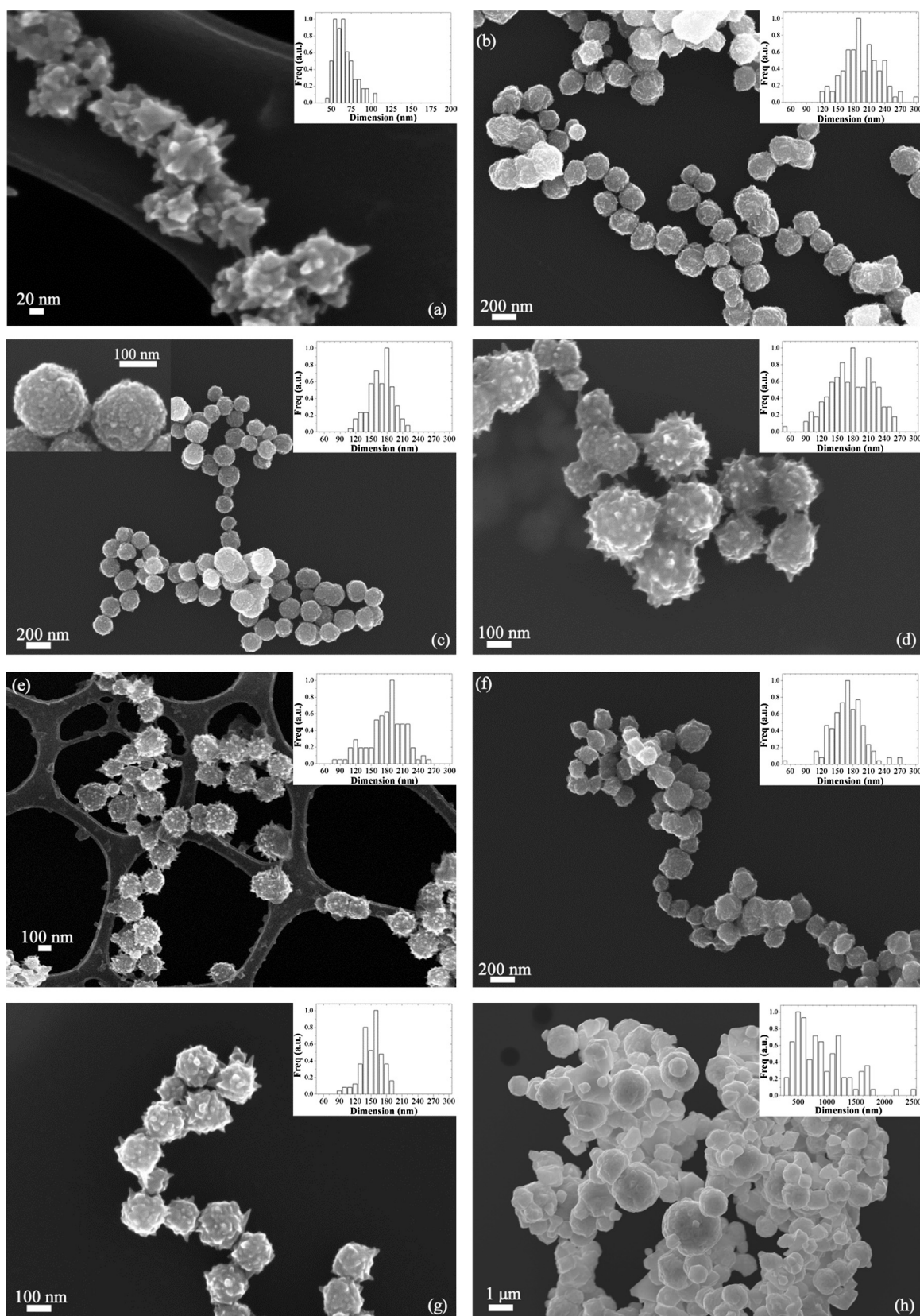


Fig. 2. SEM of Ni NPs produced by the SFTR reactor (S02 (a), S18 (b), S21 (c), S22 (d), S23 (e), and S26 (f)), a sample produced by batch reactor (B04 (g)), and the sample A01 (h). Inset in (c): high magnification of sample S02.

scope of this paper and it is currently object of a dedicated experimental activity.

Contrary to the batch synthesis, the SFTR products were always reproducible within the experimental error. This can be related to the fast heating rate of the droplets achievable with the SFTR.

For $T_R = 333$ K and $N_2H_4/Ni = 3$ a slight increasing of d_{SEM} against C_{Ni} might be claimed. Nevertheless, the values of the error bars do not allow conclusions. (S18, S19, S20, S21, S24, S25, S26, Fig. S3, Supporting Information).

The N_2H_4/Ni ratio has a clear effect on the particle surface morphology. For instance, at $T_R = 333$ K and $5 \times 10^{-2} M \leq C_{Ni} \leq 2 \times 10^{-1} M$, for $N_2H_4/Ni = 3$ the products show rather smooth surfaces (S18, S19, S20, S21), while for $N_2H_4/Ni = 20$ (S16, S23) the surface is clearly spiky, in agreement with the literature [34,59] (Section 3.3.1, Fig. 2). At $N_2H_4/Ni = 20$ complete reaction is obtained even at $T_R = 403$ K, despite the relevant gas evolution due to the N_2H_4 thermal decomposition (Eq. (5)).

The effect of aging time (t_A) was evaluated at $C_{Ni} = 5 \times 10^{-2} M$ at 343 and 368 K in the interval 1.9–11.8 min. As shown in Fig. S4 (Supporting Information), within the experimental error ($CV < 20\%$), t_A has no effect on secondary particle size. In the investigated time range, the secondary particle size is 60–70 nm (S01, S02, S03) and 180 nm (S22, S23) for $T_R = 343$ and 368 K, respectively.

A qualitative parameter to evaluate the reduction speed is the time-to-black (TtB, Table S2, Supporting Information), the time needed to turn the suspension from light-blue to black in the SFTR reactor; it represents the minimum reaction time. For instance, at $T_R = 403$ K and $C_{Ni} = 5 \times 10^{-2} M$, TtB is only 25 s (S17). As expected, the reaction speed increased for higher T_R and C_{Ni} values.

Thus, the conditions to obtain a high production rate may be calculated from C_{Ni} , P1, and TtB. For instance, in case of the samples S17 or S18, 1.1 and $2.1 g h^{-1}$ of Ni NPs were obtained, respectively, but for t_A much larger than TtB. The ratio t_A/TtB represents a time scale factor. Thus, for $C_{Ni} = 5 \times 10^{-2} M$ and $T_R = 403$ K but at higher flow rate in order to obtain $t_A = TtB$ (e.g., about 40, 40, 0, 700 $ml min^{-1}$ for P1–P4, respectively) a production of about $338 g d^{-1}$ Ni NPs is achievable with a single-tube SFTR. These flow rates are too high for available experimental set-up but an *ad-hoc* low-cost multi-tube production plant might be easily designed. Moreover, higher production rate might be possible increasing C_{Ni} .

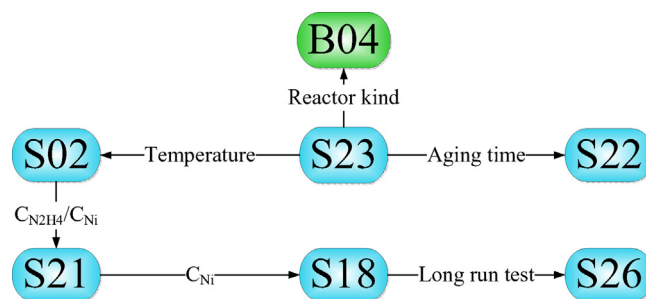
The synthesis reliability against time was tested collecting aliquots for $t_A = 15, 30, 60, 90, 180, 240, 360$ min. The secondary particle size distributions of all samples were measured from SEM pictures (Fig. S5, Supporting Information) and, in agreement with previous results on metal oxide prepared with the SFTR reactor, constant product quality was obtained over time.

3.3. Detailed characterization of selected samples

This section reports on detailed characterizations of selected samples, prepared by batch (B04), SFTR (S02, S18, S21, S22, S23, S26), and sample A01. Scheme 2 represents the applied samples selection rational and Table 1 summarizes relevant data.

3.3.1. Morphological characterization and X-ray powder diffraction (SEM, TEM, XRD, PSD)

Fig. 2g shows a SEM micrograph of a batch product (B04). The average particle size (d_{SEM}) was 150 nm ($CV = 10.1\%$) with spiky surface. HR-TEM images (Fig. 3) show a complex microstructure: the surface spikes are clearly crystalline and developed around an equiaxed core. In diluted suspensions, particles have the tendency to form chains, in agreement with previous reports [60], without an evident preferential orientation. Similar spiky surface morphologies are observed for SFTR samples. For instance, samples S02, S22, and S23 showed rough and spiky surface morphologies (Fig. 2a, d,



Scheme 2. Samples selection rational applied for the detailed characterization. The arrows show the modified parameter between two samples.

e, respectively) despite their differences in size (from 60 to 178 nm, Table 1).

As introduced in the Section 3.2, the surface morphology is strongly affected by the N_2H_4/Ni ratio. For $N_2H_4/Ni = 3$ the particles show a smoother surface independent from particle size but at higher magnification, a raspberry-like sub-structured morphology may be seen (Fig. 2b, S18, $d_{SEM} = 191$ nm; Fig. 2c, S21, $d_{SEM} = 167$ nm, inset).

Micrograph of A01 (Fig. 2h) shows that the average particles size ($>1 \mu m$) was far from the declared value (<100 nm).

X-ray diffraction patterns showed single phase *fcc*-Ni. The crystallite size was calculated from the high resolution patterns collected at the MS-X04SA beamline (Fig. 4). From Rietveld refinement lattice parameters, XRD density, crystallite size (d_{XRD}), and microstrain broadening (S_e) were calculated (Table 1). Table S4 (Supporting Information) summarize the fitting results. The crystallite size calculated with Eq. (1) resulted not much reliable: on peaks (200), (220), (311), and (400) quite similar values were calculated ($CV = 12$ – 18%) while the crystallite sizes calculated with the peak (111) and with the peak (400) were bigger 32–68% and smaller (28–35%) with respect to average values for first series of peaks, respectively. We conclude that crystallite size calculated

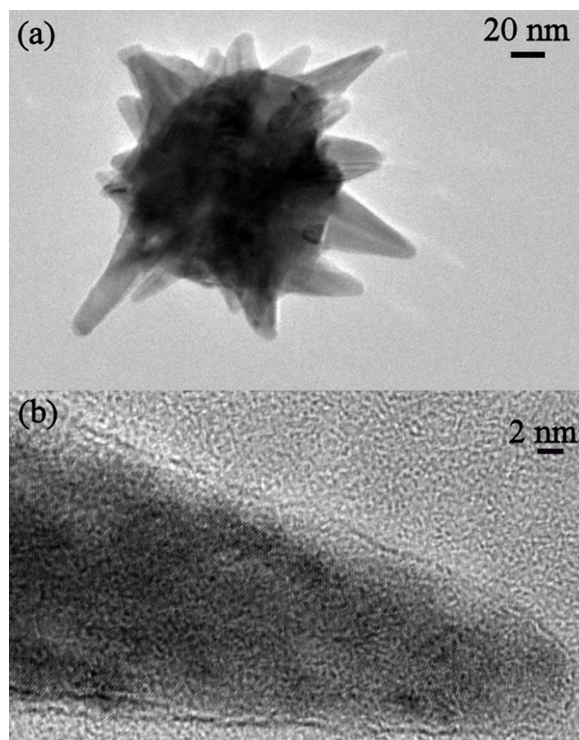


Fig. 3. (a) HRTEM image of sample B04. Inset: (b) detail of a multicrystalline spike.

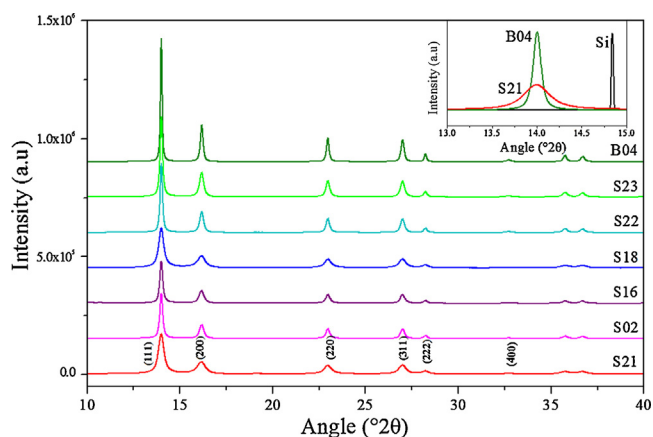


Fig. 4. High resolution X-ray powder diffraction patterns. Inset: detail of the patterns in the range 13–15° 2θ for samples S21, B04, and Si (NIST640c) used for the correction of the instrumental broadening.

using Eq. (1) and the most intense peak (1 1 1), as commonly done in literature, overestimate the crystallite size. In this paper d_{XRD} refers to value calculated by GSAS (Table 1, Table S4). Moreover, in all samples with spiky morphology, the microstrain contribution was negligible while for all raspberry-like samples was $20 \pm 1\%$. We can conclude that the particle morphology is related to a certain degree of crystallite stress.

3.3.2. Thermogravimetric analysis

Fig. 5 shows the first two oxidation–reduction cycles carried out on the samples S26 and A01. A first weight loss, in the temperature range 298–378 K, can be related to adsorbed water. A second weight loss in the temperature range 378 K and up to 503–523 K was attributed to organic residues combustion, catalyzed by Ni. At higher temperature the mass increases due to Ni oxidation to NiO: the reaction starts at 503–523 K and completed at about 703 K for all samples tested.

The thermal treatment was then completed with the NiO reduction in Ar/H₂. The reduction occurs in the temperature range 543–653 K. The consequent weight loss is coherent with the quantitative reduction of NiO to Ni, within an error <0.5 wt%. These results confirmed that at 773 K, under oxidizing condition, the samples are completely transformed to stoichiometric NiO. Thus,

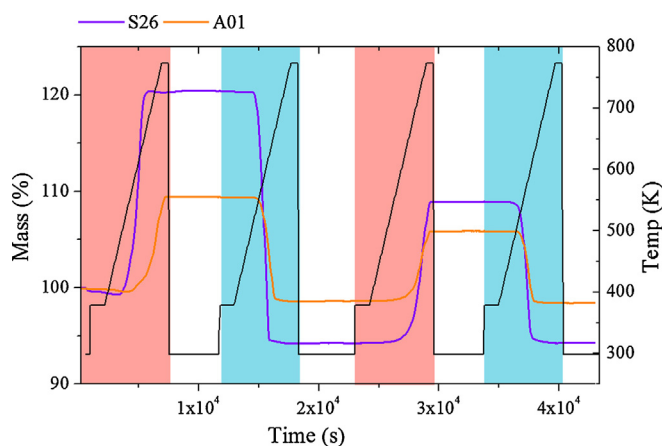


Fig. 5. Thermogravimetric analyses on samples S26 and A01. The light-red, white, and light-blue areas correspond to oxidizing (O₂ 20%/Ar), inert (Ar), and reducing (H₂ 5%/Ar) conditions, respectively. The violet, red, and black lines correspond to weight change of samples S26, A01, and the programmed temperature profile, respectively. (For interpretation of the references to color in this figure legend, the reader is referred to the web version of the article.)

Table 2

Samples composition calculated from the TGA measurements.

Sample	Composition (wt%)			
	Ni	NiO	H ₂ O	C
S02	90.69%	6.67%	1.11%	1.53%
S18	94.39%	4.73%	0.55%	0.33%
S22	96.62%	2.45%	0.49%	0.44%
S26	94.52%	4.79%	0.39%	0.29%
B04	98.16%	1.48%	0.24%	0.13%
A01	98.66%	0.95%	0.10%	29.00%

from weight variation the samples composition was calculated. The results, summarized in Table 2, are in agreement with the FTIR and XPS results (see Section 3.3.3). The TGA analyses were repeated 4 months later on powders stored in air: no detectable differences in NiO content were detected. It can be concluded that an amorphous (or at least not XRD-detectable) layer of NiO was passivating the particle surface. No clear correlations between NiO content and A_{BET} , d_{XRD} , or d_{SEM} are identified. It is worth noting that in the second oxidation cycle, the onset temperature is 150 K higher than the first run and the complete oxidation of Ni to NiO is not achieved even at 773 K (lower weight increase). As a consequence of the first thermal treatment, sintering and particle growth occurred and the oxidation onset temperature shifted towards higher values because of the thicker NiO shell formed on the solid surface. The successive cycles, a further decrease of the maximum weight increase was obtained (not showed).

Sample A01 behaved like S-series or B-series samples just after the first oxidation cycles: high oxidation onset temperature (≈ 623 K) and no complete oxidation at 773 K. In agreement with the microstructure of the exhausted samples (not shown), it can be concluded that the low reactivity is due to the rather large particle size.

3.3.3. Spectroscopic characterization and specific surface area

The products were characterized by FTIR and XPS. The FTIR spectra do not show signals attributable to organic compounds (Fig. S6, Supporting Information). These results are coherent with the limited weight loss detected by TGA (Table 2).

Fig. 6 shows the Ni 2p_{3/2} core level XPS spectra of S02, S18, S23, and B04. The dotted lines at 856.2, 853.7, and 852.6 eV were associated to Ni(OH)₂, NiO, and Ni⁰, respectively [61,62]. These results are in agreement with TGA: since Ni⁰ signal is detectable, it may be concluded that only a thin hydroxylated NiO layer is passivating the surface. In fact, 5 wt% of NiO on 150 nm particles, corresponds

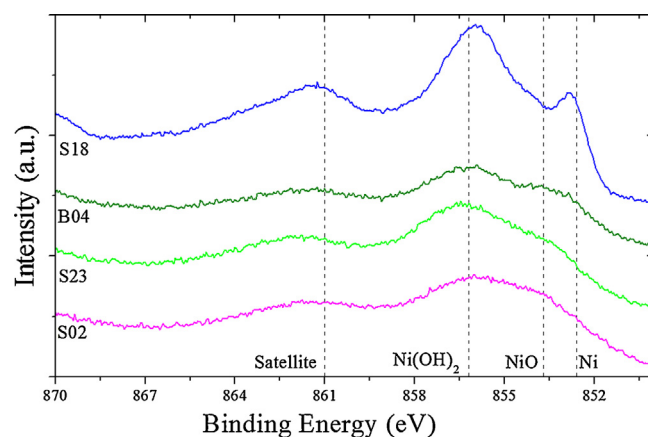


Fig. 6. Ni 2p_{3/2} core level XPS spectra recorded on samples B04, S18, S23, and S02. The vertical dotted lines correspond to binding energy of Ni⁰ (852.6 eV), NiO (853.7 eV), Ni(OH)₂ (856.2 eV) and satellite peak (861 eV).

to an oxide thickness <2 nm, which is close to the penetration depth of the XPS analysis.

Specific surface area was determined by the BET method (A_{BET} , Table 1); a rather large variation from 5.7 to 52 m² g⁻¹ was obtained. Assuming spherical Ni particles, the equivalent BET sizes were calculated (d_{BET} , Eq. (2), Table 1).

The N₂ physisorption isotherms show a clear correlation between particle size and surface morphologies. The analyzed samples may be divided in two groups (Table 1): spiky (S02, S22, S23) and raspberry-like (S18, S21, S26).

Spiky samples show H3 type slim hysteresis loops [63,64] (for instance, Fig. S7, Supporting Information) which typically corresponds to plate-like pores: in this case the associated mesoporosity may be associated with the capillary condensation among the superficial spikes. These samples are characterized by a relatively high A_{BET} and the ratio $d_{\text{BET}}/d_{\text{XRD}}$ is close to the unity. It can be concluded that these products are N₂-permeable agglomerated secondary particles with an average (numerical) size of 160–170 nm, composed by primary particles (crystallites) with an average volumetric size in the range of 11–13 nm for SFTR samples and about 19 nm for B04 (agglomeration factor, $\text{Fag} = d_{\text{SEM}}/d_{\text{XRD}}$, in the range 6–15).

Raspberry-like particles show no hysteresis in the N₂ physisorption isotherms (not shown) and a low surface area: d_{SEM} and d_{BET} are in good agreement, taking into account the surface roughness. It can be concluded that these products are not N₂-permeable agglomerated secondary particles, composed by primary particles (crystallites) of 7 nm ($\text{Fag} = 24\text{--}32$). It is worth noting that despite raspberry-like secondary particles have smaller primary particles than the spiky products, for morphological reason, a denser not N₂-permeable NiO might be formed on the surface. As consequence a rather low A_{BET} is obtained. For catalytic purpose, the NiO passivating layer may be easily removed with a mild pre-treatment under reducing atmosphere just before use.

3.3.4. Magnetic characterization

Table S3 (Supporting Information) summarizes the results of the magnetic measurements; Fig. 7 shows the results for two representative samples, S02 and S18. In case of ferromagnetic (FM) samples, at RT a quite symmetric hysteresis ($|H_c^-| \approx |H_c^+|$, where H_c is the coercive field) were measured which is coherent with the low amount of NiO detected by TGA. In fact, a relatively high amount of antiferromagnetic (AFM) NiO contamination should be revealed by an asymmetric hysteresis due to the coupling between FM core and the AFM shell [65]. The saturation magnetization (M_{sat}), close to the bulk value, are again in agreement with measured purity (TGA). The FM behavior is confirmed by the ZFC-FC analysis (inset Fig. 7a) where the maximum for the ZFC curve, i.e. the temperature at which the magnetic moment is free to change direction, is above 300 K. Sample S02 shows anhysteretic behavior (Fig. 7b), the fingerprint of superparamagnetic (SPM) particles and the ZFC-FC analysis shows a broad peak with a maximum at 180.5 K which corresponds to the blocking temperature (T_b), i.e. the temperature at which, for a given magnetic field, the transition from the free rotation of the magnetic moment to the blocked state occurs. Information on the magnetic domain can be obtained by fitting the magnetization against magnetic field with the Langevin equation (Eq. (3), Fig. 8b). The best fit was obtained considering two different particle populations in equal weight fraction and with an average size of $r_{m1} = 1.2$ ($\sigma = 0.3$) and $r_{m2} = 6$ nm ($\sigma = 0.25$).

From the Néel relaxation theory [66], the SQUID magnetometer time constant (10^2 s), and the Ni anisotropy constant (3×10^4 J m⁻³) [67], at $T_b = 180.5$ K a mean magnetic domain diameter of 15.8 nm was calculated, in good agreement with the value obtained for the bigger population found by the Langevin fit ($2r_{m2} = 12$ nm).

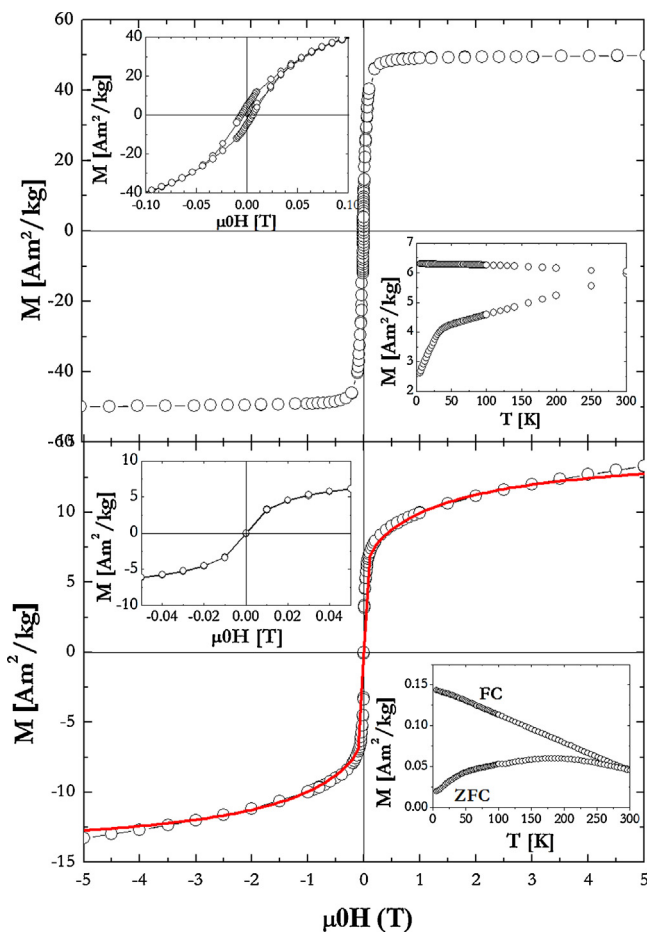


Fig. 7. SQUID measurements of samples S18 (a) and S02 (b). In both cases, the main plot represents the magnetization (M) vs. magnetic field (H) at $T = 300$ K and $\mu_0 H = 0.01$ T. The symbols are the experimental values. In (b) the red line represents the best fit according to the Eq. (3). Upper-left inset: magnification in the region close to $H = 0$. Lower-right inset: ZFC-FC curve. (For interpretation of the references to color in this figure legend, the reader is referred to the web version of the article.)

Among the spiky samples, an agreement between d_{XRD} and d_{MAG} can be lined out since to a smaller d_{XRD} corresponds a SPM behavior. The interpretation of the ferromagnetism in the raspberry-like samples is not trivial because they show d_{XRD} values below the SPM critical size. These samples show a contribution due to microstrain as well. It can be speculated that the magnetic domain may be extended over a single crystallite forming a larger multicrystalline magnetic domain. Deeper investigations are needed in order to understand the magnetic properties of these samples. Moreover, the meaning of the shoulder detected in both FM and SPM samples in the temperature range 15–45 K (Table S3, Supporting Information) is under investigation.

3.3.5. Catalytic characterization

The catalytic performance of selected Ni-NPs and A01 samples diluted in $\gamma\text{-Al}_2\text{O}_3$ were tested for the CO methanation reaction. The catalytic tests were carried out on samples with high and low A_{BET} (Table 1). Fig. S8 shows that the results for sample S02 (51.7 m² g⁻¹) and S18 (5.7 m² g⁻¹) are very similar. The possible reason for this behavior will be discussed later. Since no influence of the used Ni-NPs on the catalytic performances was detected and sample S18 was prepared in a large amount, most of the catalytic tests were carried out with S18.

The gaseous products of the reaction were CH₄, CO₂ and H₂O; no other carbon containing compounds were detected. The presence

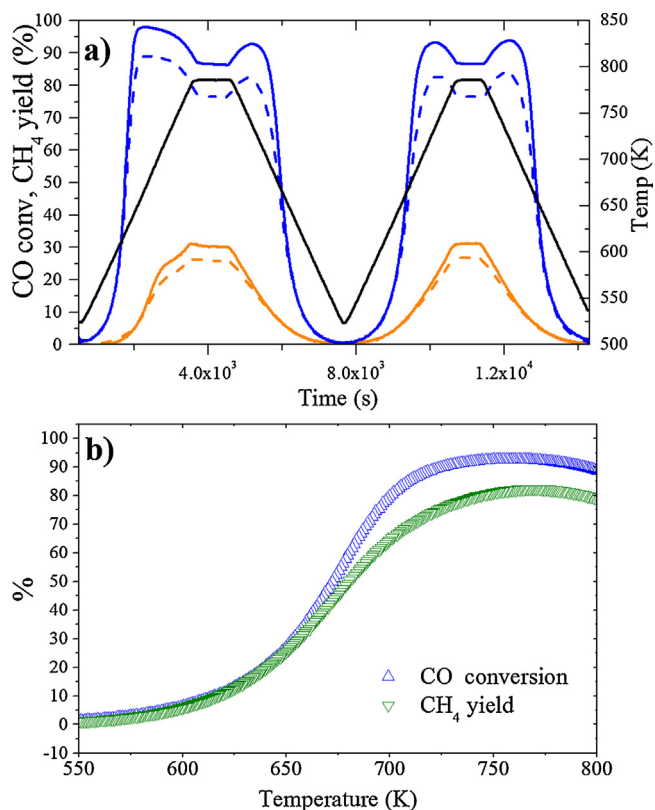


Fig. 8. CO methanation catalytic tests. (a) Gas composition vs. time for two consecutive heating-cooling cycles. Blue line: S18; Red line: A01; dashed lines: CH₄ yield; continuous lines: CO conversion; black line: measured temperature. (b) Gas composition vs. temperature for sample S18. Blue symbols: CH₄ yield; Green symbols: CO conversion. (For interpretation of the references to color in this figure legend, the reader is referred to the web version of the article.)

of CO₂ can be attributed to the water gas shift reaction. The catalytic tests were performed at the nominal temperature (i.e. the oven temperature, T_{oven}) of 593, 623, 723 and 773 K (Figs. 8 and S9), respectively.

The temperature plotted in Figs. 8 and S9, S10 (black line) is the measured temperature in the catalytic bed (T_{cat}) and it is higher than T_{oven} because of the exothermic chemical reaction.

In general, at $T_{\text{oven}} < 623$ K, the catalytic activity is initially high and slowly decays over time: this effect is particularly evident at 623 K (Fig. S9(b)).

At higher temperature, as it can be depicted from Fig. S9(c) ($T_{\text{oven}} = 723$ K) and Fig. 8 ($T_{\text{oven}} = 773$ K), the catalyst undergoes some more rapid modification and stable performances are already attained during the first cycle.

To highlight the initial transient phase, a new thermal profile was studied (Fig. S10). The catalyst shows high activity during the first heating at about $T_{\text{oven}} = 623$ K (as in Fig. S9(a)): a sharp increase in CO conversion occurs, followed by a deterioration of the efficiency over time. The temperature was then increased up to $T_{\text{oven}} = 773$ K. The catalyst completes its transformation and reaches a performance similar to those reported in Fig. 8. Then, reducing the temperature to $T_{\text{oven}} = 623$ K, the conversion drops to a value lower than during the previous plateau at the same T_{oven} . Probably this is the value obtainable after a very long ageing of pristine samples at $T_{\text{oven}} = 623$ K. The temperature then was raised step-by-step till a conversion >90% was attained. As an example of a steady-state test, $T_{\text{oven}} = 673$ K ($T_{\text{cat}} = 697$ K) has been held for a while and the obtained conversion level is close to maximum shown in Fig. S9(c) for $T_{\text{oven}} = 723$ K.

It can be concluded that a thermal treatment at relatively high temperature in *in-operando* conditions allows attaining a stable and active catalyst. Such “activation” is not shown for the catalyst prepared from A01.

Fig. 8b corresponds to the second heating ramp of Fig. 8a and shows the CO conversion and CH₄ yield against temperature. It can be seen that CO conversion in the T_{cat} range of 740–777 K is $\geq 92\%$. In the same temperature range, the CH₄ yield is $\geq 79.5\%$, with a maximum of 83% at $T_{\text{cat}} = 769$ K. At higher temperatures CO conversion and CH₄ yield decrease according to the thermodynamic equilibrium [68].

In the Fig. 8a, samples S18 and A01 are compared: the sample A01 shows CO conversion of 30.0% at $T_{\text{cat}} = 785$ K. The reason for similar activities among the tested Ni-NPs and the different reactivities of the commercial sample can be related to the observed morphologies of the powder collected after the catalytic tests (Fig. S11(a, b): sample S18; (e, f): sample S02). The images show similar micrometric sponge-like morphology for both S02 and S18 samples. Moreover, some well-faceted Ni aggregates (Fig. S11(c)), have developed, probably as a consequence of some local overheating of the catalyst *in-operando*.

Fig. S11(g, h) shows the morphology of the sample A01: the sponge-like morphology was not developed and, qualitatively, the particles size did not change much as a consequence of the catalytic test (compare with Fig. 2h). Correspondingly, the catalytic activity is rather scarce.

A coherent reactivity trend between samples S_n and A01 against temperature – this time towards oxygen for NiO formation – was shown during the TGA measurement (Fig. 5): again, almost independently to the A_{BET} values, the samples S_n were much more reactive than A01 during the first oxidation run.

We can summarize that:

- For the catalytic tests, it does not matter which S_n sample is selected because the temperature is high enough to promote particle growth in any case;
- The catalyst prepared with the samples A01 and S_n after the catalytic tests show, qualitatively, similar surface areas but the resulting activities are very different;
- There is an *in-operando* thermally-induced activation of the catalyst prepared from S_n samples, which promotes the formation a sponge-like morphology. The sponge-like catalyst is highly active, stable over time and reproducible. Such a structure is not developed by the catalyst prepared from sample A01;
- The influence of Al₂O₃ (such as Ni–Al–O interphases) or volatile Ni species (such as Ni(CO)₄) are plausible and might play a relevant role in the development of the sponge-like morphology itself.

Qualitatively, one can speculate that the good catalytic activity of the Ni-NPs-derived samples could be correlated to the developed thermally-induced sponge-like morphology. This morphology can be developed from nanoparticles only because, compared to the sample A01, they are more active towards sintering and because a higher number of particle–particle contact points are available for the 3D sponge-like morphology formation.

We can conclude that the nanometric nature of the powders, even if lost due to the thermal treatment, is a key starting point to develop the appropriate morphology of the catalyst.

Our current activity is devoted to the stabilization of the Ni-NPs towards sintering. Reaching this target implies that the catalyst may be stabilized in the pristine nanoparticulate morphology, with a behavior similar to the first heating ramp, resulting in a CO conversion of 98% at $T_{\text{cat}} \approx 687$ K and a CH₄ yield of 89.3% at $T_{\text{cat}} \approx 694$ K.

4. Summary and conclusions

A preliminary study on the most relevant synthetic parameters for the synthesis of Ni NPs in EG was carried out in the batch reactor and the obtained results were applied for the continuous production in the SFTR. The products were fully characterized by several complementary techniques and the product properties univocally identified.

By controlling the synthesis parameters, secondary particles size – in the range 50–200 nm – and particle surface morphology – spiky or raspberry-like – were tuned. Reliable and reproducible results were obtained by experiment repetition. The continuous Ni NPs production was tested up to 6 h without significant change in product properties. With the current experimental set-up the production of 3.2 g h^{-1} of 160 nm Ni NPs were obtained but the result suggests the possibility to increase the production $>300 \text{ g d}^{-1}$ in a low-cost single-tube SFTR. The feasibility of a multi-tube reactor was previously demonstrated, expanding the possibility of Ni nanopowder productions towards much larger amounts.

As expected, temperature and concentration of reactants were identified as main parameters for the particles size control but with a non-monotonous behavior, as a consequence of the competitive N_2H_4 decomposition at high temperature, was proven. Hydrazine content was identified as major parameter to control the surface morphology from raspberry-like to spiky particles. Raspberry-like secondary particles were characterized by a non N_2 -permeable hydroxylated NiO surface layer while spiky secondary particles were N_2 -permeable with a limited mesoporosity, attributed to capillary condensation among spikes. In both cases, a sub-structure of much smaller primary particles (8–16 nm) was identified by XRD. Primary particles size may be tuned as well in order to obtain a ferromagnetic or superparamagnetic products.

The thermal behavior in air and the catalytic properties towards CO methanation were studied. Thermal analysis was used to quantify the oxidation state of particles surface as well as their thermal stability and oxidation threshold in air. The catalytic tests were mainly carried out with powders produced by SFTR (S18) and compared with commercial powders provided by Aldrich (A01), both mixed with γ -alumina. Sample S18 showed a stable CH_4 yield (83% at 769 K) while sample A01 showed a lower CH_4 yield (26% at 785 K). The reason of the huge difference in performance is associated to the sponge-like morphology that the nanopowder-derived catalysts develop *in-operando*.

The catalytic properties of the produced Ni NPs were still far from the best commercial catalyst available but this work represents the first step toward the continuous production of advanced metal catalysts with carefully tuned properties. According to a similar approach, advanced bimetallic nanopowders catalysts as well as core-shell nanopowders with anti-sintering properties are currently under development.

Author contributions

The manuscript was written through contributions of all authors.

Funding sources

The first author (MAL) thanks the University of Genoa and the Paul Scherrer Institute for the financial support for the long stay period at PSI. Financial support was obtained from the CCMX NanoAir project and the SNF project no. 144302.

Acknowledgments

We thank Dr. Luca Quaroni, Dr. Christian Proff, Mr. Albert Schuler, Mr. Erich De Boni, and Dr. Mauro Michetti for their contribution to the samples characterization. The XRD and FTIR data were collected at the X01DC and X04SA-MS beamlines of the Swiss Light Source (PSI).

Appendix A. Supplementary data

Supplementary data associated with this article can be found, in the online version, at <http://dx.doi.org/10.1016/j.apcatb.2014.03.045>.

References

- [1] P. Misra, *Handbook of Metal Physics, Metallic Nanoparticles*, Elsevier, New York, 2009.
- [2] E.L. Wolf, M. Medikonda, *Understanding the Nanotechnology Revolution*, Wiley, New York, 2012.
- [3] H.H. Delavari, H.R. Madaah Hosseini, M. Wolff, J. Magn. Magn. Mater. 335 (2013) 59.
- [4] B. Panella, A. Vargas, A. Baiker, J. Catal. 261 (2009) 88.
- [5] J. Ge, Q. Zhang, T. Zhang, Y. Yin, *Angew. Chem.* 120 (2008) 9056.
- [6] R.B.N. Baig, R.S. Varma, *Chem. Commun.* 49 (2013) 752.
- [7] M. Ye, Q. Zhang, Y. Hu, J. Ge, Z. Lu, *Chem. Eur. J.* 16 (2010) 6243–6250.
- [8] S. Parveen, R. Misra, S.K. Sahoo, *Nanomedicine* 8 (2012) 147.
- [9] M. Zahmakiran, S. Ozkar, *Nanoscale* 3 (2011) 3462.
- [10] C.S.S.R. Kumar, F. Mohammad, *Adv. Drug Deliv. Rev.* 63 (2011) 789.
- [11] X. Yang, X. Wang, G. Gao, E. Liu, Q. Shi, J. Zhang, C. Han, J. Wang, H. Lu, J. Liu, M. Tong, *Int. J. Hydrogen Energy* 38 (2013) 13926.
- [12] J. Gao, C. Jia, M. Zhang, F. Gu, G. Xu, F. Su, *Catal. Sci. Technol.* 3 (2013) 2009.
- [13] G. Garbarino, P. Riani, M.A. Lucchini, F. Canepa, S. Kawale, G. Busca, *Int. J. Hydrogen Energy* 38 (2013) 82.
- [14] N. Yan, C. Xiao, Y. Kou, *Coord. Chem. Rev.* 254 (2010) 1179–1218.
- [15] G.A. Bhaduri, L. Siller, *Catal. Sci. Technol.* 3 (2013) 1234–1239.
- [16] H. Zhao, H. Song, L. Chou, *Inorg. Chem. Commun.* 15 (2012) 261.
- [17] P. Riani, M.A. Lucchini, G. Garbarino, F. Canepa, G. Busca, *J. Mol. Catal. A-Chem.* 383–384 (2014) 10.
- [18] A. Testino, *Int. J. Appl. Ceram. Technol.* 10 (2013) 723.
- [19] H.G. Kim, J.I. Park, G.H. Lee, *Mater. Chem. Phys.* 140 (2013) 419.
- [20] Y.L. Hou, S. Gao, *J. Alloy Compd.* 365 (2004) 112.
- [21] K.P. Donegan, J.F. Godsell, D.J. Otway, M.A. Morris, S. Roy, J.D. Holmes, *J. Nanopart. Res.* 14 (2012) 670.
- [22] M.A. Domínguez-Crespo, E. Ramírez-Meneses, V. Montiel-Palma, A.M. Torres Huerta, H. Dorantes Rosales, *Int. J. Hydrogen Energy* 34 (2009) 1664.
- [23] R. Eluri, B. Paul, *Mater. Lett.* 76 (2012) 36.
- [24] D. Li, S. Komarneni, *J. Am. Ceram. Soc.* 89 (2006) 1510.
- [25] S. Amoroso, G. Ausanio, C. De Lisio, V. Iannotti, M. Vitiello, X. Wang, L. Lanotte, *Appl. Surf. Sci.* 247 (2005) 71.
- [26] V.M. Rao, C.H. Castano, J. Rojas, A.J. Abdulghani, *Radiat. Phys. Chem.* 89 (2013) 51.
- [27] K. Chou, K. Huang, *J. Nanopart. Res.* 3 (2001) 127.
- [28] C. Jiang, G. Zou, W. Zhang, W. Yu, Y. Qian, *Mater. Lett.* 60 (2006) 2319.
- [29] P.K. Khanna, P.V. More, J.P. Jawalkar, B.G. Bharate, *Mater. Lett.* 63 (2009) 1384.
- [30] K.J. Carroll, J.U. Reveles, M.D. Shultz, S.N. Khanna, E.E. Carpenter, *J. Phys. Chem. C* 115 (2011) 2656.
- [31] G.G. Couto, J.J. Klein, W.H. Schreiner, D.H. Mosca, A.J. De Oliveira, A.J.G. Zarbin, *J. Colloid Interface Sci.* 311 (2007) 461.
- [32] S.H. Wu, D.H. Chen, *J. Colloid Interface Sci.* 259 (2003) 282.
- [33] R.J. Joseyphus, T. Matsumoto, H. Takahashi, D. Kodama, K. Tohji, B. Jayadevan, *J. Solid State Chem.* 180 (2007) 3008.
- [34] L. Bai, F. Yuan, Q. Tang, *Mater. Lett.* 62 (2008) 2267.
- [35] T. Hinotsu, B. Jayadevan, C.N. Chinnasamy, K. Shinoda, K. Tohji, *J. Appl. Phys.* 95 (2004) 7477.
- [36] R. Eluri, B. Paul, *J. Nanopart. Res.* 14 (2012) 800.
- [37] H. Wang, X. Kou, J. Zhang, J.B. Li, *Mater. Sci.* 31 (2008) 97.
- [38] J. Lemaitre, N. Jongen, R. Vacassy, P. Bowen, *US Patent* 6,458,335, 2002.
- [39] R. Vacassy, J. Lemaitre, H. Hofmann, J.H. Gerlings, *AIChE J.* 46 (2000) 1241.
- [40] P. Bowen, M. Donnet, A. Testino, M. Viviani, M.T. Buscaglia, V. Buscaglia, P. Nanni, *Key Eng. Mater.* 206 (2002) 21.
- [41] S. Guillemet-Fritsch, *Solid State Ionics* 171 (2004) 135.
- [42] M. Donnet, N. Jongen, J. Lemaitre, P. Bowen, *J. Mater. Sci. Lett.* 19 (2000) 749.
- [43] N. Jongen, *Chem. Eng. Technol.* 26 (2003) 303.
- [44] A. Testino, *PhD Thesis*, University of Genoa, 2004.
- [45] M.N. Kashid, W.D. Agar, *Chem. Eng. J.* 131 (2007) 1.
- [46] A. Aimable, N. Jongen, A. Testino, M. Donnet, J. Lemaitre, H. Hofmann, P. Bowen, *Chem. Eng. Technol.* 34 (2011) 344.
- [47] J.W. Park, E.H. Chae, S.H. Kim, J.H. Lee, J.W. Kim, S.M. Yoon, J.Y. Choi, *Mater. Chem. Phys.* 97 (2006) 371.
- [48] N.R.N. Roselina, A. Azizan, *Procedia Eng.* 41 (2012) 1620.

- [49] P.R. Willmott, D. Meister, S.J. Leake, M. Lange, A. Bergamaschi, M. Böge, M. Calvi, C. Cancellieri, N. Casati, A. Cervellino, Q. Chen, C. David, U. Flechsig, F. Gozzo, B. Henrich, S. Jäggi-Spielmann, B. Jakob, I. Kalichava, B. Karvinen, J. Krempasky, A. Lüdeke, R. Lüscher, S. Maag, C. Quitmann, M.L. Reinle-Schmitt, T. Schmidt, P. Schmitt, A. Streun, I. Vartiainen, M. Vitins, X. Wang, R. Wulfschleger, *J. Synchrotron Rad.* 20 (2013) 667.
- [50] A.C. Larson, R.B. Von Dreele, General Structure Analysis System (GSAS), Technical Report LAUR 86-748, Los Alamos National Laboratory, New Mexico, 2000.
- [51] Inorganic Crystal Structure Database (ICSD), Fachinformationzentrum Karlsruhe and Gemlin Institute, Karlsruhe 1997: Ni # 41508.
- [52] GSAS Manual (<http://www.ccp14.ac.uk/solution/gsas/>).
- [53] S. Brunauer, P. Emmett, E. Teller, *J. Am. Chem. Soc.* 60 (1938) 309.
- [54] E. Barrett, L. Joyner, P. Halenda, *J. Am. Chem. Soc.* 73 (1951) 373.
- [55] D.A. Shirley, *Phys. Rev. B* 5 (1972) 4709.
- [56] D. Chen, S. Wu, *Chem. Mater.* 13 (2000) 1354.
- [57] J.W. Park, E.H. Chae, S.H. Kim, J.H. Lee, J.W. Kim, S.M. Yoon, J.-Y. Choi, *Mater. Chem. Phys.* 97 (2006) 371.
- [58] J. Baumgartner, A. Dey, P.H.H. Bomans, C. Le Coadou, P. Fratzl, N.J.M. Sommerdijk, D. Faivre, *Nat. Mater.* 12 (2013) 310.
- [59] C.F. Goh, H. Yu, S.S. Yong, S.G. Mhaisalkar, F.Y.C. Boey, P.S. Teo, *Mater. Sci. Eng. B* 117 (2005) 153.
- [60] F. Ma, Q. Li, J. Huang, J. Li, *J. Cryst. Growth* 310 (2008) 3522.
- [61] H.W. Nesbitt, D. Legrand, G.M. Bancroft, *Phys. Chem. Min.* 27 (2000) 357.
- [62] S. D'Addato, V. Grillo, S. Altieri, R. Tondi, S. Valeri, S. Frabboni, *J. Phys. Condens. Mater.* 23 (2011) 175003.
- [63] S.J. Gregg, K.S.W. Sing, Adsorption, Surface Area and Porosity, Academic Press, 1995.
- [64] K.S.W. Sing, D.H. Everett, R.A.W. Haul, L. Moscou, R.A. Pierotti, J. Rouquérol, T. Siemieniewska, *Pure Appl. Chem.* 57 (1985) 603.
- [65] S.K. Sharma, J.M. Vargas, M. Knobel, K.R. Pirota, C.T. Meneses, S. Kumar, C.G. Lee, P.G. Pagliuso, C. Rettori, *J. Appl. Phys.* 107 (2010) 09D725.
- [66] I. Prigogine, S.A. Rice, W.T. Coffey, P.J. Cregg, Y.U.P. Kalmykov, *Adv. Chem. Phys.* 83 (1993) 68.
- [67] E.P. Wohlfarth, *Ferromagnetic Materials*, Vol. 1, North Holland Pub. Company, 1980.
- [68] J. Gao, Y. Wang, Y. Ping, D. Hu, G. Xu, F. Gu, F. Su, *RSC Adv.* 2 (2012) 2358.